PROCEEDINGS, 43rd Workshop on Geothermal Reservoir Engineering
Stanford University, Stanford, California, February 12-14, 2018
SGP-TR-213

Effect of Coupled Porothermoelastic Stress on Shear Stimulation of Enhanced Geothermal Systems

Zhiqiang Fan and Rishi Parashar

Desert Research Institute, Reno, NV 89512, United States

E-mail Zhiqiang.fan@dri.edu

Keywords: thermoporoelastic, hydraulic stimulation, fault reactivation

ABSTRACT

Cost-effective extraction of heat from enhanced geothermal systems (EGS) depends highly on the successful hydraulic stimulation of geothermal reservoirs. Wide field observations of microseismicity during hydraulic stimulation of EGS when the injection pressure is far below the magnitude of least in situ stress suggest that hydroshearing may be the primary mechanism of induced permeability enhancement. Long time delay between the start of hydraulic stimulation and the onset of seismicity highlights the importance of incorporating thermal stress in stability analysis of preexisting fractures and faults. To better understand the mechanism of shear stimulation in EGS and to address the role of thermal stress in changing shear potential of fractures, with superposition technique we analyzed the stress and pore pressure changes due to injection of cold fluid into a hot geothermal reservoir under different stress regimes incorporating fully coupled porothermoelasticity. The results show that at early time, thermoelastic stress due to the shrinkage of rock matrix is mainly confined to the vicinity of injection wells, whereas poroelastic stress duo to matrix deformation influences a larger region. The temperature front lags behind the pore pressure front. Cooling induced thermoelastic stress counteracts to the poroelastic stress. With increasing time of injection, thermoelastic stress plays a more dominant role in shearing fractures. Depending on the relative orientation of fractures with respect to the in situ stress and magnitude of in situ stress, the direction of shear migration is controlled by the transient competition between poroelastic stress and thermoelastic stress.

1. INTRODUCTION

Since its debut in the 1970s at Fenton Hill, enhanced geothermal system (EGS) has attracted much interest due to its technical feasibility and potential of cost-effective extraction of geothermal energy. The sustainable and cost-competitive heat mining from EGS depends highly on the successful hydraulic stimulation of reservoirs where massive cold fluid is pumped at high rate and pressure to enhance permeability and porosity by opening/reactivating preexisting faults and fractures thus allowing fluid circulation through the reservoirs. Predicting the behavior of geothermal reservoirs under hydraulic stimulation is critical for better utilization of EGS. Wide observation of microseismicity when bottom-hole pressure is less than the minimum principal stress and downward migration of microsesimicity during hydraulic stimulation (Pine & Batchelor, 1984) suggest that hydroshearing may be a viable mechanism in EGS stimulation (Tester et al., 2006; McClure & Horne, 2014) .

Injection induced pore pressure and stress perturbations as well as thermal stress due to the temperature difference between the injected fluid and native fluid changes the stability of preexisting faults. It is commonly assumed that fault slip follows the Coulomb failure criterion, i.e., when the shear stress overcomes the frictional resistance, slip occurs. Under tension positive convention, Coulomb criterion can be expressed by

$$CFS = \tau - \mu(\sigma_n + p) \tag{1}$$

where CFS is the Coulomb failure stress, μ is coefficient of friction, p is pore fluid pressure, τ and σ_n are shear and total normal stresses acting on the fault, respectively. Equivalently, we can use slip tendency T_s to characterize the spatiotemporal stability, defined as

$$T_s = \frac{\tau}{\sigma_n + p} \geq \mu \tag{2}$$

An advantage to using slip tendency as an indicator of fault stability is that it is dimensionless. While previous studies in thermoporoelasticity focused on borehole with pore pressure and traction boundary conditions (Li at al., 1998; Abousleiman & Ekbote, 2005), to the best knowledge of the authors, the analytical solution for fluid injection at constant rate in the framework of fully coupled thermoporoelasticity is unavailable. We solve the time-dependent stress and pore pressure for a wellbore subjected to a constant flux and far field in situ stress. Our goal is to quantify the transient slip tendency of faults due to the stress and pore pressure changes associated with hydraulic stimulation.

The rest of the paper is organized as follows. Section 2 presents the constitutive and governing equations for fully coupled thermoporoelasticity. Section 3 formulates the boundary and initial value problem and derives the analytical solutions in Laplace domain. Section 4 gives the numerical results and examines the contributions from the poroelastic stress and thermal stress to the hydroshearing of preexisting faults. Section 5 concludes the paper.

2. GOVERNING EQUATIONS FOR THERMOPOROELASTICITY

For a homogeneous, isotropic thermoporoelastic porous material, the constitutive equations are given by (Mctigue, 1986; Kurashige, 1989)

$$\varepsilon_{ij} = \frac{1+\nu}{E}\sigma_{ij} - \frac{\nu}{E}\sigma_{kk}\delta_{ij} + \frac{\alpha p}{3K}\delta_{ij} + \alpha_s T\delta_{ij} \tag{3}$$

$$\varsigma = \frac{\alpha}{KB}\left(\frac{B\sigma_{kk}}{3} + p\right) - \varphi\left(\alpha_f - 3\alpha_s\right)T \tag{4}$$

where ε_{ij} is strain, σ_{ij} is stress, σ_{kk} is the bulk stress, p is pore pressure, T is the temperature change, ζ is the increment of fluid content, and δ_{ij} is the Kronecker delta. The material constants given above are: the Young's modulus E, the drained Poisson's ratio ν, the Biot coefficient α, the linear thermal expansion coefficient of solid matrix α_s, the Skempton's coefficient B, the bulk modulus of fluid-saturated rock K, the volumetric thermal expansion coefficient of the pore fluid $\alpha_{f.}$ and porosity φ. Compared to the counterpart in poroelasticity, thermoporoelasticity introduces three additional constants : φ, α_f and α_s. In addition to the constitutive equations, transport and conservation equations are needed to derive the governing equations for fully coupled thermoporoelasticity.

Momentum balance

$$\sigma_{ji,j} = 0 \tag{5}$$

Fluid mass balance

$$\frac{\partial \varsigma}{\partial t} + q_{k,k} = 0 \tag{6}$$

Energy conservation

$$\rho C\frac{\partial \mathrm{T}}{\partial t} + h_{k,k} = 0 \tag{7}$$

Darcy's law

$$q_i = -\frac{k}{\mu}p_{,i} \tag{8}$$

Fourier's law

$$h_i = -\kappa T_{,i} \tag{9}$$

In the above equations, q is the fluid flux, k is intrinsic permeability, μ is pore fluid viscosity, ρ and C are the mass density and specific heat capacity, respectively, h is the heat flux, and κ is the thermal conductivity. Solving the stress components from constitutive equations (3) and (4), substituting them into the equilibrium equations (5), and expressing strain in terms of displacement derivative yield the governing equations for displacements (Cheng, 2016)

$$G\nabla^2 u_i + \frac{G}{1-2\nu}\varepsilon_{kk,i} = \alpha p_{,i} + \frac{E\alpha_s T_{,i}}{1-2\nu} \tag{10}$$

Substituting the Fourier's law into the energy conservation equation gives the heat diffusion equation

$$\frac{\partial \mathrm{T}}{\partial t} = c_h\nabla^2 T \tag{11}$$

The pore pressure diffusion equation can be obtained by substituting Darcy's law into the fluid mass balance equation and using constitutive equations (Abousleiman & Ekbote, 2005)

$$\frac{\partial p}{\partial t} - \frac{k}{\mu}M\nabla^2 p = -\alpha M\frac{\partial \varepsilon_{kk}}{\partial t} + M\left[\phi\left(\alpha_f - 3\alpha_s\right) + 3\alpha\alpha_s\right]\frac{\partial T}{\partial t} \tag{12}$$

where M is the Biot Modulus.

$$M = \frac{BK_u}{\alpha} = \frac{BK}{\alpha(1-\alpha B)} \tag{13}$$

For an axisymmetric deformation, the deformation filed is decoupled from the fluid and heat diffusion and equation (12) can be simplified as

$$\frac{\partial p}{\partial t} - c\nabla^2 p = c^{'} \frac{\partial T}{\partial t} \tag{14}$$

where

$$c = \frac{k}{\mu} \frac{2GB^2(1+\nu_u)^2(1-\nu)}{9(1-\nu_u)(\nu_u-\nu)} \tag{15}$$

$$c^{'} = \frac{c}{k/\mu}\left[\phi(\alpha_f - 3\alpha_s) + \frac{6\alpha_s(\nu_u-\nu)}{B(1-\nu)(1+\nu_u)}\right] \tag{16}$$

3. PROBLEM FORMULATION AND ANALYTICAL SOLUTIONS

Consider a wellbore of radius a in an infinite thermoporoelastic rock matrix as shown in Figure 1. The wellbore surface is subjected to a constant fluid flux q_w and a constant temperature T_w which is colder than the virgin formation temperature T_0. In the far field, the wellbore is under the in situ stress, the hydrostatic pore pressure p_0 and the constant temperature $T_{0_\circ}$ The boundary conditions are given as follows.

On the borehole surface (r = a),

$$\sigma_r = -p_w H(\mathrm{t});\ \sigma_{r\theta} = 0;\ q_r = q_w H(\mathrm{t});\ T = T_w H(\mathrm{t}) \tag{17}$$

where H(t) is the Heaviside function, $q_w = -\frac{k}{\mu}\frac{dp}{dr}$ is the fluid flux at the borehole wall, T_w is the temperature of injected fluid, and p_w is the time-dependent fluid pressure required to keep a constant fluid flux at the wellbore, which is unknown a priori. It is worth noting that we consider a Neumann boundary value problem (flux specified) compared to previous studies considering a Dirichlet boundary (pore pressure specified).

At the far field ($r \to \infty$),

$$\sigma_x = -S_{h\min};\ \sigma_y = -S_{H\max};\ p = p_0;\ \ T = T_0 \tag{18}$$

where S_{hmin} and S_{Hmax} are the minimum and maximum horizontal in situ stress, respectively, and p_0 and T_o are the virgin pore pressure and temperature, respectively. Equivalently, the boundary conditions at the far field can be expressed as

$$\sigma_r = -P_0 + \mathrm{S}_0\cos 2\theta;\ \sigma_{r\theta} = -\mathrm{S}_0\sin 2\theta;\ p = p_0;\ T = T_0 \tag{19}$$

where $P_0 = \frac{\mathrm{S}_{H\max} + S_{h\min}}{2}$ and $S_0 = \frac{\mathrm{S}_{H\max} - S_{h\min}}{2}$.

To make the complex problem solvable, following Detounay and Cheng (1988) and Li et al. (1998), we decompose the loads into three loading modes and superpose the solutions to the three individual sub-problems to obtain the solution for the complex problem. The boundary conditions at the wellbore surface for the *induced* stress, fluid flux, and temperature for the three sub-problems are given as follows.

Mode 1:

$$\sigma_r^{(1)} = -(p_w - P_0)H(\mathrm{t});\ \sigma_{r\theta}^{(1)} = 0;\ q_r^{(1)} = 0;\ T^{(1)} = 0 \tag{20}$$

Mode 2:

$$\sigma_r^{(2)} = 0;\ \sigma_{r\theta}^{(2)} = 0;\ q_r^{(2)} = q_w H(\mathrm{t});\ T^{(2)} = (T_w - T_0)H(\mathrm{t}) \tag{21}$$

Mode 3:

$$\sigma_r^{(3)} = -S_0 \cos 2\theta \; H(t); \;\; \sigma_{r\theta}^{(3)} = S_0 \sin 2\theta \; H(t); \;\; q_r^{(3)} = 0; \;\; T^{(3)} = 0 \tag{22}$$

Mode 1 represents the mechanical loading resulting from hydrostatic part of far filed stress and normal stress at the wellbore. Mode 2 loading accounts for the fluid flux and temperature changes in a coupled way. Mode 3 considers the deviator stress from far filed loading.

At the far field, the *induced* stress, pore pressure and temperature are zero. Apply Laplace transform to the governing equations (10), (11) and (14) and boundary conditions (20) -(22), we can get the analytical solutions in the Laplace domain.

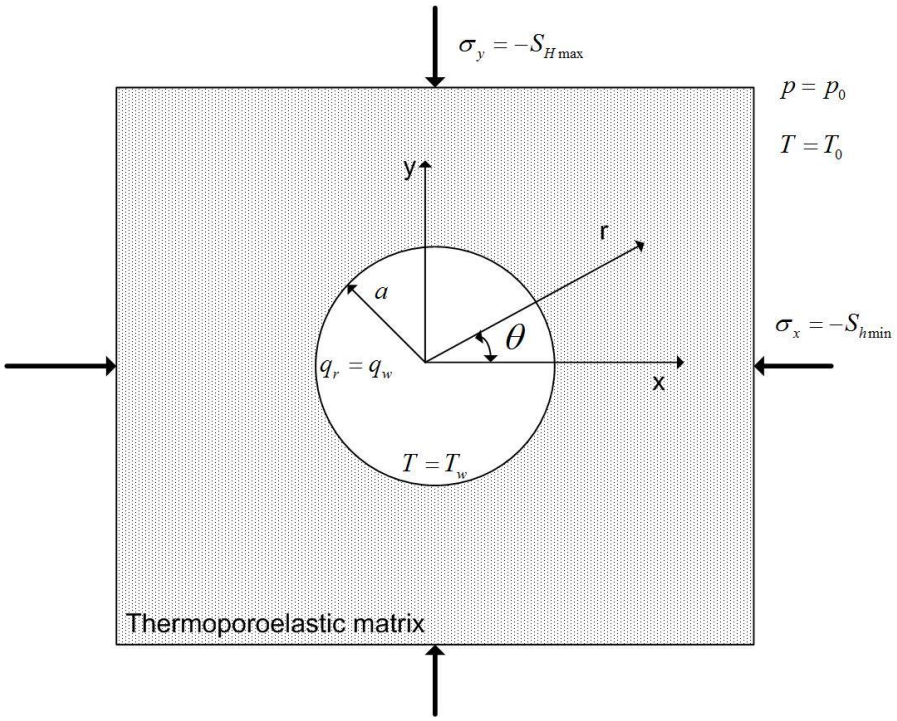

Figure 1. A wellbore of radius *a* subjected to fluid flux q_w , temperature T_w, and far field in situ stress. The injected fluid temperature T_w is different from native formation temperature T_0.

The solutions for mode 1 loading are given by

$$T^{(1)} = 0 \tag{23}$$

$$p^{(1)} = 0 \tag{24}$$

$$\frac{k\sigma_r^{(1)}}{q_w \mu a} = -\frac{k(p_w - p_0)}{q_w \mu a}\frac{a^2}{r^2} \tag{25}$$

$$\frac{k\sigma_\theta^{(1)}}{q_w \mu a} = \frac{k(p_w - p_0)}{q_w \mu a}\frac{a^2}{r^2} \tag{26}$$

$$\sigma_{r\theta}^{(1)} = 0 \tag{27}$$

where p_w is the time-dependent fluid pressure which can be determined from mode 2 solutions.

The solutions for mode 2 in the Laplace domain are given by

$$\frac{s\tilde{T}^{(2)}}{T_w - T_0} = \frac{K_0(\xi_h)}{K_0(\beta_h)} \tag{28}$$

$$\frac{\tilde{p}^{(2)} ks}{q_w \mu a} = \frac{c^{"}(T_w - T_0)}{q_w a(1 - c/c_h)}(F4 - F6) + F5 \tag{29}$$

$$\frac{\tilde{\sigma}_r^{(2)}ks}{q_w\mu a}=\frac{2\eta c^{"}\left(T_w-T_0\right)}{q_w a\left(1-c/c_h\right)}\left(F1-F2\right)-2\eta F3-\frac{Ek\alpha_s\left(T_w-T_0\right)}{q_w\mu a\left(1-\nu\right)}F2 \tag{30}$$

$$\begin{aligned}\frac{\tilde{\sigma}_\theta^{(2)}ks}{q_w\mu a}&=\frac{2\eta c^{"}\left(T_w-T_0\right)}{q_w a\left(1-c/c_h\right)}\left(F2-F1-F4+F6\right)+2\eta\left(F3-F5\right)\\&\quad+\frac{Ek\alpha_s\left(T_w-T_0\right)}{q_w\mu a\left(1-\nu\right)}\left(F2-F4\right)\end{aligned} \tag{31}$$

$$\sigma_{r\theta}^{(2)}=0 \tag{32}$$

where

$$\eta=\frac{\alpha\left(1-2\nu\right)}{2\left(1-\nu\right)} \tag{33}$$

$$F1=\frac{\sqrt{c/c_h}K_1\left(\beta_h\right)\left[\beta K_1\left(\beta\right)-\xi K_1\left(\xi\right)\right]}{\xi^2K_0\left(\beta_h\right)K_1\left(\beta\right)} \tag{34}$$

$$F2=\frac{\beta_hK_1\left(\beta_h\right)-\xi_hK_1\left(\xi_h\right)}{\xi_h^2K_0\left(\beta_h\right)} \tag{35}$$

$$F3=\frac{\beta K_1\left(\beta\right)-\xi K_1\left(\xi\right)}{\beta\xi^2K_1\left(\beta\right)} \tag{36}$$

$$F4=\frac{K_0\left(\xi_h\right)}{K_0\left(\beta_h\right)} \tag{37}$$

$$F5=\frac{K_0\left(\xi\right)}{\beta K_1\left(\beta\right)} \tag{38}$$

$$F6=\frac{\sqrt{c/c_h}K_1\left(\beta_h\right)K_0\left(\xi\right)}{K_0\left(\beta_h\right)K_1\left(\beta\right)} \tag{39}$$

$$\beta=a\sqrt{s/c};\ \ \beta_h=a\sqrt{s/c_h};\ \ \xi=r\sqrt{s/c};\ \ \xi_h=r\sqrt{s/c_h};c^{"}=\frac{c^{'}k}{\mu} \tag{40}$$

Here tides denote the Laplace transform, s is the transform variable, and K_0 and K_1 are modified Bessel function of second kind of order zero and order 1, respectively.

From equation (29), we can get the Laplace transform of p_w

$$\left.\frac{\tilde{p}_w^{(1)}ks}{q_w\mu a}\right|_{r=a}=\frac{c^{"}\left(T_w-T_0\right)}{q_w a\left(1-c/c_h\right)}\left[1-\frac{\sqrt{c/c_h}K_1\left(\beta_h\right)K_0\left(\beta\right)}{K_0\left(\beta_h\right)K_1\left(\beta\right)}\right]+\frac{K_0\left(\beta\right)}{\beta K_1\left(\beta\right)} \tag{41}$$

Inverting (41) and substitute it into (25) and (26), we can get the induced stress field for mode 1 loading.

The solutions for mode 3 are given by (Detournay and Cheng, 1988)

$$T^{(3)}=0 \tag{42}$$

$$\tilde{p}^{(3)}=\frac{S_0\cos 2\theta}{s}\left[\frac{c\mu}{2Gk}C_1K_2\left(\xi\right)+\frac{C_2B\left(1+\nu_u\right)}{3\left(1-\nu_u\right)}\frac{a^2}{r^2}\right] \tag{43}$$

$$\tilde{\sigma}_r^{(3)} = \frac{S_0 \cos 2\theta}{s}\left\{\frac{B(1+\nu_u)}{3(1-\nu_u)}C_1\left[\frac{6K_2(\xi)}{\xi^2}+\frac{K_1(\xi)}{\xi}\right]-\frac{C_2}{1-\nu_u}\frac{a^2}{r^2}-3C_3\frac{a^4}{r^4}\right\} \tag{44}$$

$$\tilde{\sigma}_\theta^{(3)} = \frac{S_0 \cos 2\theta}{s}\left\{-\frac{B(1+\nu_u)}{3(1-\nu_u)}C_1\left[\left(\frac{6}{\xi^2}+1\right)K_2(\xi)+\frac{K_1(\xi)}{r\sqrt{s/c}}\right]+3C_3\frac{a^4}{r^4}\right\} \tag{45}$$

$$\tilde{\sigma}_{r\theta}^{(3)} = \frac{S_0 \sin 2\theta}{s}\left\{\frac{2B(1+\nu_u)}{3(1-\nu_u)}C_1\left[\frac{3K_2(\xi)}{\xi^2}+\frac{K_1(\xi)}{\xi}\right]-\frac{C_2}{2(1-\nu_u)}\frac{a^2}{r^2}-3C_3\frac{a^4}{r^4}\right\} \tag{46}$$

The constants C_1, C_2 and C_3 are determined from the boundary conditions and given by

$$C_1 = \frac{-24\beta(1-\nu_u)(\nu_u-\nu)}{B(1+\nu_u)(D_2-D_1)} \tag{47}$$

$$C_2 = \frac{4(1-\nu_u)D_2}{D_2-D_1} \tag{48}$$

$$C_3 = -\frac{D_2+D_1+16(\nu_u-\nu)K_2(\beta)/\beta}{D_2-D_1} \tag{49}$$

$$D_1 = 4(\nu_u-\nu)K_1(\beta) \tag{50}$$

$$D_2 = \beta(1-\nu)\left[\beta K_1(\beta)+2K_2(\beta)\right] \tag{51}$$

Superposing solutions from mode 1 to mode 3 to the original temperature, pore pressure and stress field yields the final solution to the overall problem at hand.

$$T = T_0 + T^{(2)} \tag{52}$$

$$p = p_0 + p^{(2)} + p^{(3)} \tag{53}$$

$$\sigma_r = -P_0 + S_0 \cos 2\theta + \sigma_r^{(1)} + \sigma_r^{(2)} + \sigma_r^{(3)} \tag{54}$$

$$\sigma_\theta = -P_0 - S_0 \cos 2\theta + \sigma_\theta^{(1)} + \sigma_\theta^{(2)} + \sigma_\theta^{(3)} \tag{55}$$

$$\sigma_{r\theta} = -S_0 \sin 2\theta + \sigma_{r\theta}^{(3)} \tag{56}$$

4. NUMERICAL RESULTS

Inversion of Laplace transform is applied using Stehfest's algorithm to obtain the numerical results in the time domain (Detournay and Cheng, 1988). This section illustrates the effects of coupled thermoporoelastic stress and pore pressure on fault slip due to hydraulic stimulation. The material parameters for a typical granite used in the numerical analysis is listed in Table 1 (McTigue, 1990; Clauser, 1992; Wang, 2000). We assume that a wellbore of radius 0.1 m is subjected to fluid flux at an injection rate of 20 l/s. The stimulation interval length H is assumed to be 200 m. The constant temperature of injected fluid T_0 is 20 °C and the formation temperature is 120 °C at a depth of 2 km. The in situ stress is characterized by S_V = 23 MPa/km, S_{Hmax}=18.4 MPa/km, and S_{hmin} = 14.7 MPa/km. The initial hydrostatic pore pressure gradient is assumed to be 10 MPa/km.

Figure 2 shows the evolution normalized radial stress $k\sigma_r^{(1)}/\mu a q_w$ and hoop stress $k\sigma_\theta^{(1)}/\mu a q_w$ as a function of radial distance at different times of t* for mode 1 loading ($t^* = ct/a^2$). The normalized time t^* characterize the typical hydraulic diffusion time. It can be seen both induced stresses decrease quickly with increasing distance from the wellbore. Unlike the case where wellbore is subjected constant pore pressure, the hoop stress increases progressively with time. We not that the induced hoop stress is compressive because p_w is still under P_0, the far field hydrostatic stress.

Figures 3 and 4 show the normalized temperature change $T^{(2)}/(T_w - T_0)$ and normalized pore pressure change $kp^{(2)}/\mu a q_w$ versus normalized radial distance at different times of t* for mode 2 loading, respectively. The induced pore pressure and temperature increase with increasing time and decrease with increasing radial distance from the wellbore. But the temperature front falls far behind the pore pressure front because the thermal diffusivity is significantly less than the hydraulic diffusivity. As a result, at early time, pore pressure

increase plays a dominant role in affecting fault stability compared to thermal stress and thermal stress effect is only confined in a limited region near the wellbore. It is interesting to note that the pore pressure at the wellbore surface increases with time.

Table 1 Material parameters used in the numerical analysis

Symbols	Definition	Value(unit)
Poroleastic		
G	Shear modulus	15 GPa
ν	Drained Poison's ratio	0.25
K	Drained bulk modulus	25 GPa
α	Biot coefficient	0.47
B	Skempton coeffcient	0.85
Hydraulic		
k	Permeability	1 mD
μ	Viscosity	3.0×10^{-4} Pa-s
φ	Porosity	0.01
Thermal		
C_h	Thermal diffusivity	1.1×10^{-6} m2s^{-1}
κ	Thermal conductivity	2.5 Wm^{-1}K^{-1}
α_s	Solid linear expansion coefficient	8×10^{-6} K^{-1}
α_f	Fluid volumetric expansion coefficient	7×10^{-4} K^{-1}

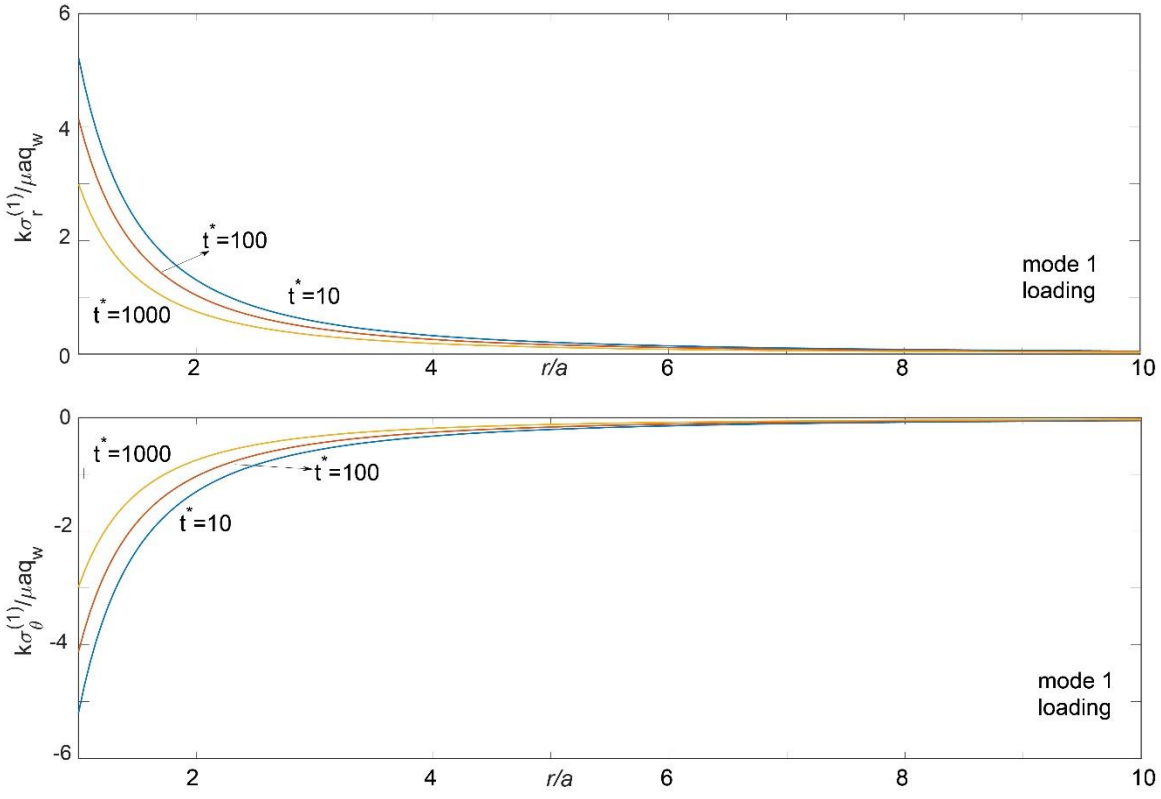

Figure 2. Normalized radial stress $k\sigma_r^{(1)}/\mu aq_w$ and hoop stress $k\sigma_\theta^{(1)}/\mu aq_w$ vs. normalized radial distance at different times of t* (t*= ct/a2) for mode 1 loading.

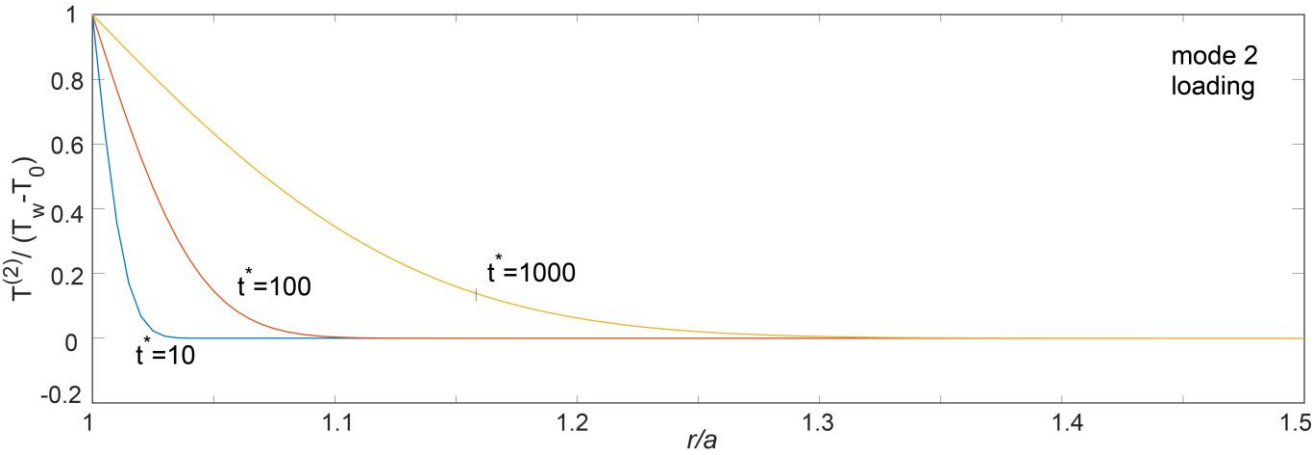

Figure 3. Normalized induced temperature $T^{(2)}/(T_w - T_0)$ vs. normalized radial distance at different times of t* for mode 2 loading.

Figure 5 and 6 show the distribution of normalized radial stress $k\sigma_r^{(2)} / \mu a q_w$ and hoop stress $k\sigma_\theta^{(2)} / \mu a q_w$ as a function of radial distance at different times of t* for mode 2 loading. For a specific time, the radial stress initially decreases, reaches a peak, and then increases with increasing radial distance. We notice the peak of the radial stress is located within the rock and not on the borehole surface. As time goes on, the radial stress becomes more compressive due to the constant flux boundary conditions.

Figure 7 shows the distribution of induced pore pressure as a function of radial distance at different times of t* along the θ = 0° direction for mode 3 loading. The contribution to the pore pressure increase from mode 3 loading is negligibly small compared to that from mode 2. Since mode 1 loading does not induce any pore pressure changes, the pore pressure changes is governed by mode 2 loading.

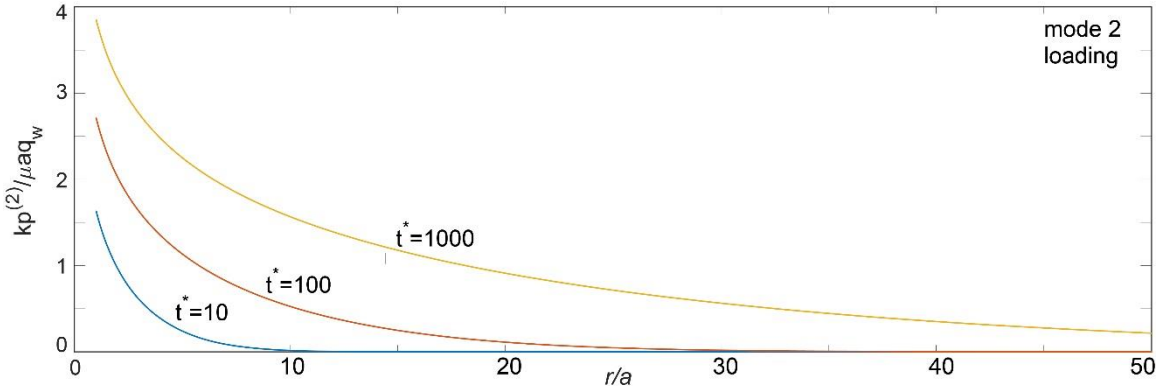

Figure 4. Normalized induced pore pressure $kp^{(2)} / \mu a q_w$ vs. normalized radial distance at different times of t* for mode 2 loading.

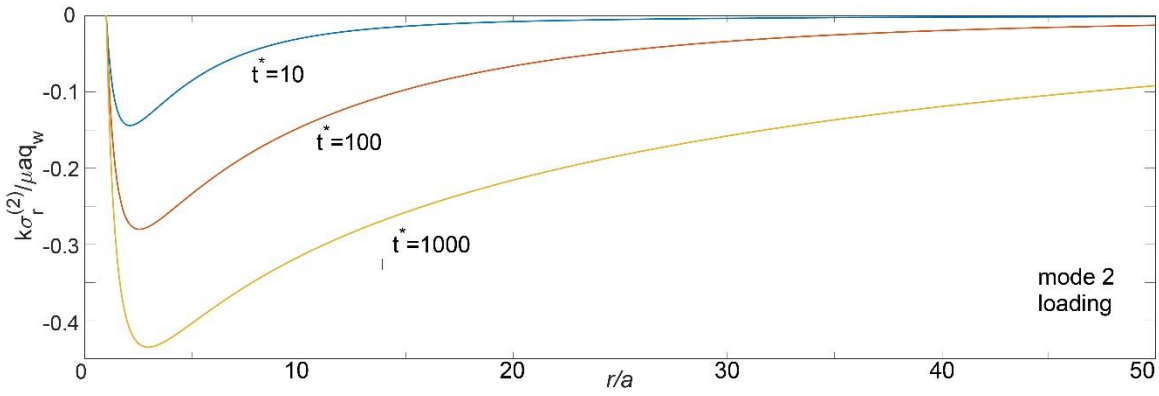

Figure 5. Normalized induced normal stress $k\sigma_r^{(2)} / \mu a q_w$ vs. normalized radial distance at different times of t* for mode 2 loading.

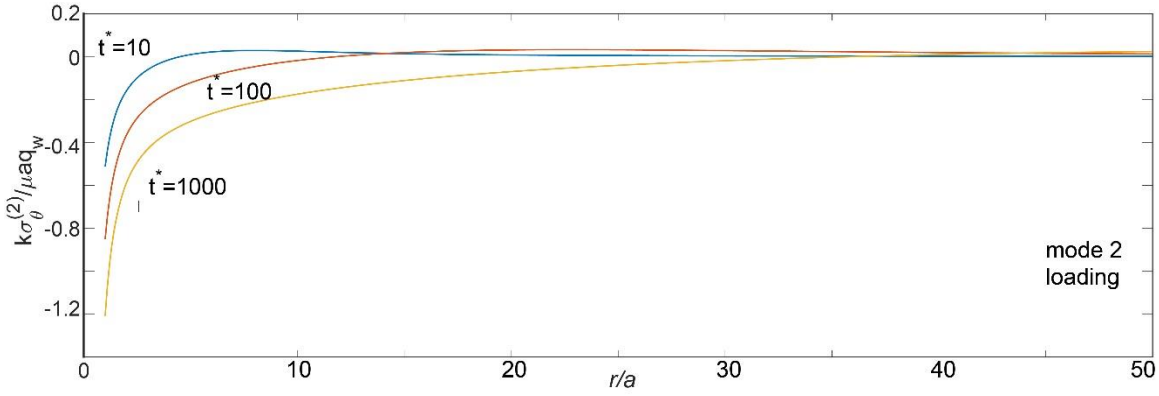

Figure 6. Normalized induced hoop stress $k\sigma_\theta^{(2)} / \mu aq_w$ vs. normalized radial distance at different times of t* for mode 2 loading.

For illustration purposes, we show the time dependent changes in slip tendency for different radial distance from the wellbore. We assume that in the normal faulting stress regime considered here, there are preexisting optimally oriented faults relative to the prevailing in situ stress which strikes parallel to S_{Hmax} with a dip angle of 60°. When the slip tendency reaches the coefficient of friction (0.6), fault reactivation occurs. It is clear that hydraulic stimulation is more effective in the vicinity of the wellbore mainly due to the more pronounced thermoporoelastic effects near the wellbore region. The increasing pore pressure due to injection decreases the effective normal stress acting on the fault, and reduces the slip resistance (Fan et al., 2016). Figure 9 shows the time required to reactivate the optimally oriented faults as a function of distance from the wellbore for a coefficient of friction of 0.6. As anticipated, delayed reactivation of fault with increasing distance from the wellbore is mainly due to the quick decay of pore pressure.

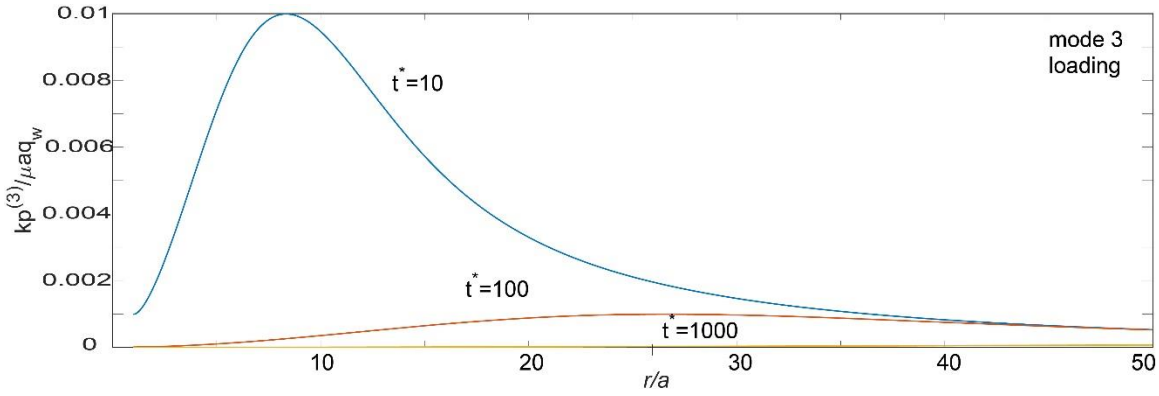

Figure 7. Normalized induced pore pressure $kp^{(3)} / \mu aq_w$ vs. normalized radial distance at different times of t* for mode 3 loading.

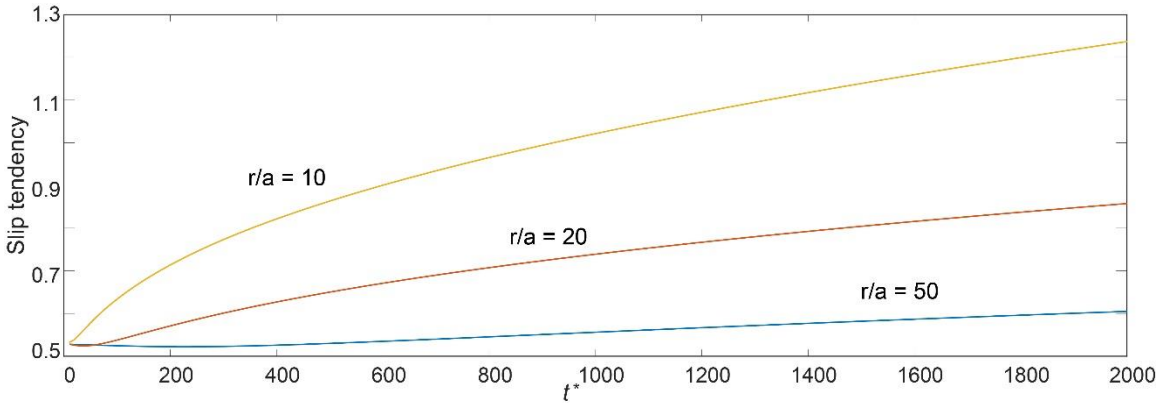

Figure 8. Evolution of slip tendency as a function of time for different radial distance from the wellbore

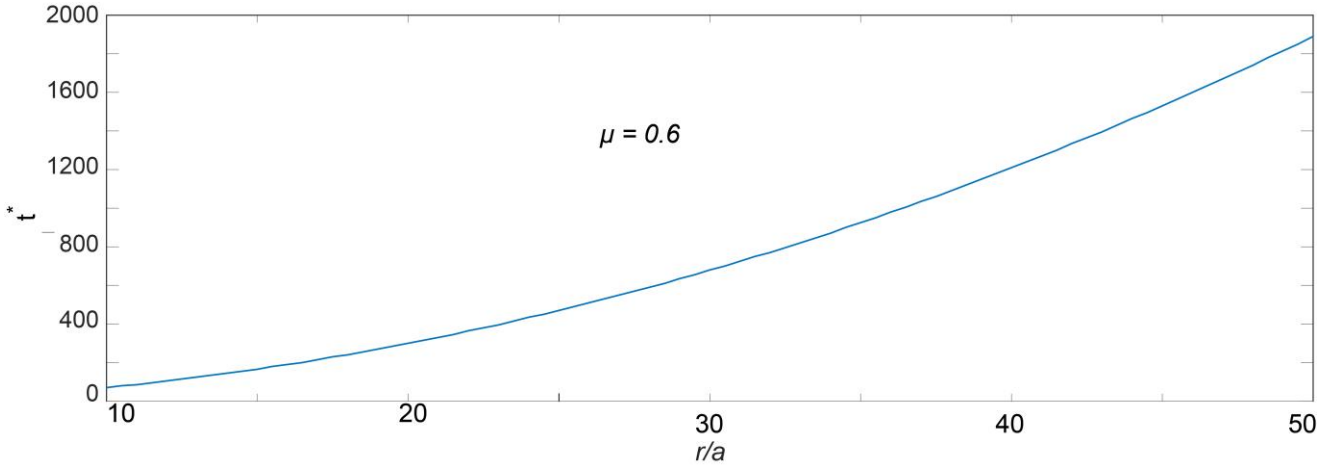

Figure 9. Moment of fault reactivation as a function of radial distance from the wellbore for a coefficient of friction of 0.6

5. CONCLUSIONS

Analytical solutions are presented for temperature, pore pressure and stress field in Laplace domain for a wellbore subjected to fluid flux on wellbore surface and far field in situ stress. Using load decomposition approach, the problem is subdivided into 3 sub-problems. Numerical results are shown for solutions in the time domain to investigate the effects of thermoporoelastic coupling on shear stimulation of preexisting faults. Based on the numerical solutions, we reach the following conclusions:

(1) There are two distinct fronts associated with the thermoporoelastic coupling problem: one for fluid diffusion, and one for thermal diffusion, characterized by the hydraulic diffusivity and thermal diffusivity, respectively. For the current problem, since hydraulic diffusivity is much higher than thermal diffusivity, the temperature front lags far behind the pore pressure front. Thermal stress plays an effective role only in the vicinity of the wellbore. The competition between the two fronts depends on the ratio between hydraulic diffusivity and thermal diffusivity.

(2) The pore pressure induced by the far field stress is negligible small compared to that induced by fluid injection into the wellbore.

(3) Shear stimulation is most effective in the vicinity of the wellbore. Slip tendency decreases with increasing distance from the wellbore.

(4) Time required to reactivate the faults increases with increasing distance from the wellbore for optimally oriented faults of the same orientation.

ACKNOWLEDGEMET

The first author is supported by a fellowship from Neil J Redfield Foundation.

REFERENCES

Abousleiman, Y. and S. Ekbote (2005). Solutions for the inclined borehole in a porothermoelastic transversely isotropic medium. Journal of applied Mechanics 72(1): 102-114.

Cheng, A. H. D. (2016). Poroelasticity (Vol. 27). Switzerland: Springer.

Clauser, C. (1992). Permeability of crystalline rocks. Eos, Transactions American Geophysical Union, 73(21), 233-238.

Detournay, E., & Cheng, A. D. (1988). Poroelastic response of a borehole in a non-hydrostatic stress field. International Journal of Rock Mechanics and Mining Sciences & Geomechanics Abstracts 25(3): 171-182).

Fan, Z., Eichhubl, P., & Gale, J. F. (2016). Geomechanical analysis of fluid injection and seismic fault slip for the Mw4. 8 Timpson, Texas, earthquake sequence. Journal of Geophysical Research: Solid Earth, 121(4), 2798-2812.

Kurashige, M. (1989). A thermoelastic theory of fluid-filled porous materials. International Journal of Solids and Structures 25(9): 1039-1052.

Li, X., Cui, L., & Roegiers, J. C. (1998). Thermoporoelastic modelling of wellbore stability in non-hydrostatic stress field. International Journal of Rock Mechanics and Mining Sciences, 35(4-5), 584.

McClure, M. W., & Horne, R. N. (2014). An investigation of stimulation mechanisms in Enhanced Geothermal Systems. International Journal of Rock Mechanics and Mining Sciences, 72, 242-260.

McTigue, D. (1986). Thermoelastic response of fluid-saturated porous rock. Journal of Geophysical Research: Solid Earth 91(B9): 9533-9542.

McTigue, D. (1990). Flow to a heated borehole in porous, thermoelastic rock: Analysis. Water Resources Research 26(8): 1763-1774.

Pine, R. J., & Batchelor, A. S. (1984). Downward migration of shearing in jointed rock during hydraulic injections. International Journal of Rock Mechanics and Mining Sciences & Geomechanics Abstracts, 21(5): 249-263.

Tester, J. W., Anderson, B. J., Batchelor, A. S., Blackwell, D. D., DiPippo, R., Drake, E., & Petty, S. (2006). The future of geothermal energy: Impact of enhanced geothermal systems (EGS) on the United States in the 21st century. Massachusetts Institute of Technology, 209.

Wang, H. F. (2000). Theory of linear poroelasticity, Princeton University Press Princeton, NJ.